Escherichia coli sister cells dynamically organize developmental rosettes

Devina Puri[1] and Kyle R. Allison[1,2,3]

[1]*Biomedical Engineering, Emory University and Georgia Institute of Technology*
[2]*Infectious Diseases, Department of Medicine, Emory University School of Medicine*
[3]*Emory Antibiotic Resistance Center, Department of Medicine, Emory University School of Medicine*

Correspondence: Kyle R. Allison; kyle.r.allison@emory.edu

Author Contributions: DP performed experiments and analyses. DP & KRA designed experiments, interpreted results, and wrote the manuscript.

Competing Interests: Authors have filed a provisional patent related to the growth devices used in this study.

This PDF includes:

Main Text
Figures 1 to 3

Abstract

Rosettes are self-organizing, circular multicellular communities that initiate the development of organs and embryos in higher organisms. Their formation results from the active repositioning of adhered sister cells and is thought to distinguish multicellular organisms form unicellular ones (1). Though biofilms have been argued to be the result of microbial development (2), bacterial rosettes are uncommon and largely uncharacterized (3-7). Here we report that *Escherichia coli* rosettes form by a consistent and novel mechanism. After division, sister cells "folded" to reposition themselves in parallel. After the second division, cells folded again to produce clonal 4-cell, *quatrefoil* rosettes. Analysis of folding revealed that it followed an angular random walk, comprised of ~1-µm angular strokes and directional randomization. We further showed that this motion was produced by the flagellum, the extracellular tail whose rotation generates swimming motility. Rosette formation was found to require *de novo* flagella synthesis and the balancing of sister-cell adhesion and propulsion. Moreover, by interrupting sister-cell folding, we demonstrated that rosette formation was required for *E. coli*'s multicellular-chain life cycle and the resulting clonal-chain biofilms. This study establishes that a unicellular bacterium self-organizes developmental rosettes by active sister-cell repositioning, and has implications for the evolution of multicellularity as well as *E. coli*'s roles as a commensal and pathogenic organism.

33 **Main Text**

34 We recently reported that *Escherichia coli* can form biofilms by a microscopic life cycle that has
35 multiple, genetically-regulated stages (3, 8) (Fig. S1-2). Early in this process, individual cells
36 grow into 4-cell *quatrefoil* rosette-like communities that partially enclose an internal space 1 μm
37 in diameter and 2 μm long (3). As rosettes extend into chains, the enclosed-space configuration is
38 maintained by production of the extracellular matrix (ECM) (3), similar to ECM production during
39 transition of mammalian rosettes to developmental lumens (9). These chains remain clonal, *i.e.*
40 descendant from a single ancestral cell, and attach to surfaces and become dormant once they
41 contain ~1,000 cells. *Ag43* facilitates the adherence of sister cells, though this alone does not
42 explain the robust formation of quatrefoil configurations, perhaps indicating sister cells reposition
43 themselves into rosettes. Given the separate time scales of chain morphogenesis (hours) and
44 rosette formation (minutes or less), our previous study documented rosettes but did not reveal how
45 they formed. In this study, we combine microscopy, genetics, and quantitative analyses to
46 characterize the motion of individual cells and reverse engineer rosette formation in *E. coli*.

47 Using recently-developed growth devices and time-lapse microscopy (3), we recorded the
48 motion of individual *E. coli* cells (model commensal strain MG1655) by both bright field and
49 fluorescence microcopy. These devices were developed to study the early events of hydrostatic
50 biofilm formation (3) and allow tracking of unattached cells without perturbing fluid flow. The
51 resulting videos revealed rosettes form in a consistent manner (Movies S1-2). After division, sister
52 cells adhered to each other at their new poles. After ~10 minutes of negligible motion, cells
53 "folded" onto one another, pivoting about their adhered poles to align parallel (Fig. 1A). This
54 folding took place in under one minute and was comprised of angular movements interspersed
55 with pauses. 2-cell "doublets" then grew and synchronously divided creating 4-cell groups, which
56 folded while keeping their poles in contact to produce quatrefoil rosettes. No additional folding

57 took place after 4-cell rosettes had formed (Fig. 1B). Instead, cells continued to adhere at their
58 poles after division and transitioned into longitudinally growing chains while approximately
59 keeping quatrefoil configuration. These findings demonstrate that 4-cell quatrefoil rosettes are
60 generated by sister-cell folding at the 2-cell and 4-cell stages. This sister-cell folding may provide
61 the mechanism for the intracellular rosettes in urinary tract infections (UTIs) (10) and, combine
62 with the stabilizing role of the ECM (3), explains the defined structure of *E. coli* multicellular
63 chains.

64 To quantify folding, we next fluorescently imaged cells containing green fluorescent
65 protein to enable image processing methods (GFP) (Fig. 1C; Fig. S3-8; Movies S3-7) and
66 calculated the 2-dimensional angle between sister cells (θ) (Fig. S9). Changes in θ were small
67 immediately after division, but greatly increased as sister cells folded into parallel orientation (Fig.
68 S9 & 11). Circumferential rotation of cells around their long axis ("spinning") (Movie S3) was
69 noted during pauses, again indicating folding results from two types of motion: angular movements
70 and paused spinning. We calculated the delay period between cell division and the onset of folding
71 to be ~13 minutes (Fig. S11). The maximum angular speed was >6°/s, the detection limit based
72 on the 30-second imaging rate (Fig. S10-11). These findings demonstrate that sister-cell folding
73 is comprised of two distinct motions and is regulated relative to the cell cycle, but also indicate
74 that faster, three-dimensional data will be required.

75 To further quantify sister-cell folding, we recorded bright-field videos at 2-second
76 resolution (Fig. S12-16; Movies S8-12), and tracked the position of cell poles. The angle between
77 a cell and the cover glass (Φ) can be imputed by trigonometry from the cell's length and 2D-
78 projection. Together, θ and Φ values fully specify the 3-dimensional angle between sister cells.
79 Calculated θ dynamics (Fig. 1D; S17) were consistent with the fluorescent data (Fig. S11),

80 revealing delayed-onset sister-cell folding. The average maximum angular speed of θ was
81 calculated to be ~36°/s (Fig. S18). Φ dynamics (Fig. S19) were similar to θ dynamics and
82 significant changes in Φ and θ coincided (Fig. 1E; Fig. S20). The angular trajectories of sister
83 cells (plotting Φ against θ) suggested folding may perform an angular random walk (Fig. 1F; Fig.
84 S21). We calculated trajectories of the un-adhered cell poles in Cartesian coordinates, which also
85 suggested random-walk motion (Fig. 1G; Fig. S22-23) and illustrated that folding resulted from
86 switching between angular strokes and paused directional randomization. Inter-stroke pause times
87 fit a long-tail distribution (Fig. S24) with similar time scales to rotational switching of the
88 flagellum (11-13) which produces a random walk during swimming motility (14, 15). Stroke
89 distance was 0.8-1.2 μm (Fig. 1H), though increased to ~2 μm in some cells before folding ended.
90 The angle between consecutive strokes (δ) was found to be uncorrelated (r=-0.041; n=59) and near
91 uniformly distributed (Fig. 2I; Fig. S25) satisfying the criteria for a simple random walk (16).

92 We hypothesized that sister-cell folding was generated by the flagellum (17, 18), an
93 extracellular tail that is rotated like a propeller by a molecular motor to produce swimming motility
94 (Fig. 2A). The flagellum and its motor are required for hydrostatic biofilms, but the importance
95 of directional switching of the motor is less clear (19, 20). Swimming had not been observed
96 during biofilm-generating chain morphogenesis (3), suggesting the flagellum might perform an
97 alternate role in repositioning cells. To investigate this, we tracked non-motile Δ*fliC* and Δ*motA*
98 strains (Movies S13-14). Δ*fliC* cells lack the main protein in the tail while Δ*motA* cells lack a
99 motor component and are deficient in propulsion. Initially, Δ*fliC* and Δ*motA* cells behaved
100 similarity to wild-type: they grew, divided, and adhered at their poles (Fig. 2B & D). However,
101 neither Δ*fliC* nor Δ*motA* cells produced angular movements or folded into rosettes. Instead, Δ*fliC*
102 and Δ*motA* cells grew in linear, single-cell-wide chains (Fig. 2C & E). Quantifying θ demonstrated

103 negligible angular motion in Δ*fliC* and Δ*motA* cells (Fig. 2F & G). Angular motion at the 2-cell
104 and 4-cell stages in wild-type, and its lack in Δ*fliC* and Δ*motA*, was further demonstrated by
105 quantifying community length, which suddenly halves when sister-cell folding occurs (Fig. 2H;
106 Fig. S26). These findings demonstrate that rosette formation results from active flagella-mediated
107 sister-cell folding. Flagella-mediated sister-cell repositioning is also the mechanism of rosette
108 formation in marine eukaryote *Salpingoeca rosetta*, a model for early multicellular organisms (21).
109 *E. coli* and *S. rosetta* do not share habitats or evolutionary histories and their similar mechanisms
110 of rosette formation may indicate common underlying rules of multicellularity.

111 The flagellum can rotate in both the clockwise (CW) and counterclockwise (CCW)
112 directions, causing tumbling and linear swimming, respectively. We hypothesized that CW and
113 CCW directions separately produced angular strokes and directional randomization during folding.
114 To test this, we used Δ*cheY* (mainly CCW) and Δ*cheZ* (mainly CW) mutants (22, 23). Videos
115 demonstrated that the Δ*cheY* mutation abolished angular stokes (Fig. S26-30; Movies S15-17).
116 However, some Δ*cheY* cells "pushed" past each other to align in parallel, though with an opposite
117 polar orientation to folding. This push motion resembled the expected CCW-generated swimming
118 of this strain. Quantifying motion of Δ*cheY* sister cells revealed that travel distance remained <0.6
119 μm (Fig. 2I) and was comparable to the random motion of wild-type cells before they began folding
120 (Fig. 2I, inset). Additionally, sister-cell angular trajectories in Δ*cheY* further demonstrated that
121 angular strokes were abolished and illustrated that pushing rather than folding was responsible
122 when parallel alignment occurred (Fig. 2J). We next tracked Δ*cheZ* sister cells and found that this
123 mutation abolished the pauses between angular strokes (Fig. S31-34; Movies S18-20). Moreover,
124 Δ*cheZ* sister cells often forcibly separated, blocking community formation (Fig. S35). Quantifying
125 sister-cell motion and angular trajectories further demonstrated that Δ*cheY* mutation abolished the

126 pauses and caused cell separation (Fig. 2I & K). Together, these findings confirm that angular
127 strokes result from CW rotation and paused directional randomization results from CCW rotation
128 during sister-cell folding. This reflects an inversion of the functional roles in chemotaxis where
129 CCW rotation causes linear swimming and CW rotation causes tumbling.

130 Though these findings demonstrate the roles of CW and CCW rotation in sister-cell
131 folding, their contributions to community formation are less apparent. For example, exclusive CW
132 rotation can separate sister cells and block rosette formation. Moreover, CCW's role is unclear as
133 CW should sufficiently span the angular space and align cells. This suggests CCW switching may
134 serve to "brake" angular motion and thereby prevent sister-cell separation and is important to the
135 robustness of rosette formation. To further explore this, we determined the relative amounts of
136 different community types in these strains after several generations (Fig. S36), and found that
137 ~83% of wild-type, ~29% of Δ*cheZ,* ~0% of Δ*cheY* communities were rosettes or rosette-like
138 chains and the remainder of communities were either single-cell-wide chains or non-rosette
139 aggregates. Hence, rotational switching is critical to robust rosette folding, but is not absolutely
140 required for community formation. These results are consistent with past data indicating
141 differences between flagella and chemotaxis genes in hydrostatic biofilm formation (19, 20, 24,
142 25). A recent study suggested *E. coli* can combine *Ag43* adhesion and AI-2-based chemotaxis to
143 form polyclonal aggregates (24). Though possible in cases, our data show that this does not occur
144 during clonal rosette formation.

145 Sister-cell separation by unchecked CW rotation (Δ*cheZ* cells) suggested propulsion can
146 overcome adhesion and that rosette formation might require intermediate forces. The flagellum's
147 force corresponds to the number motor subunits and the tail length (17, 18). Resultantly, force
148 during *de novo* flagella synthesis in unflagellated cells begins at a minimum and increases to strong

149 propulsion by mature flagella generations later (26). We hypothesized that cells with mature
150 flagella would separate after division and investigated this using a motile strain (AW405) that is
151 closely related to MG1655. Flagellation in AW405 is controlled by glucose, due to a mutation
152 causing CRP-regulation of the flagella master regulator *flhDC* (27). By fluorescent staining (28),
153 we confirmed flagellation's dependence on glucose in this strain (Fig. 3A). Next, tracking
154 flagellated AW405 cells in glucose (-) conditions, we observed swimming cells and that all sister
155 cells separated after division (Fig. 3B; Movie S21). Even after many generations, no folding,
156 rosettes, or multicellular communities were observed. To verify the flagellum's role, we tracked
157 AW405 cells with a Δ*fliC* mutation in glucose (-) conditions and observed sister cells remained
158 adhered at their poles, producing linear, single-cell-wide chains (Fig. 3C; Movie S22) identical to
159 those of MG1655 Δ*fliC* and Δ*motA* cells. Consistent with the Δ*cheZ* data, these findings indicate
160 that sister cells are separated by strong flagella propulsion. These findings may also explain why
161 the greater forces of "fluid-flow" impair biofilm formation by commensal *E. coli* (29).

162 These findings are an additional indication that sister-cell folding may rely on the
163 intermediate forces produced during *de novo* flagella biosynthesis (26). Therefore, inducing
164 flagellation in unflagellated AW405 cells might cause them to fold into rosettes. To test this, we
165 grew AW405 cells in glucose (+) media then loaded them into hydrostatic, glucose (-) conditions
166 to induce flagella biosynthesis. In these experiments, sister cells folded at both the 2-cell and 4-
167 cell stages, thereby producing quatrefoil rosettes identically to MG1655 (Fig. 3D; Movie S23).
168 These results show that rosette folding is dependent on *de novo* flagella biosynthesis and support
169 the idea that sister cells *balance* the forces of repositioning and adhesion to form rosettes (Fig. 3E).

170 Though rosettes were observed at the beginning of *E. coli*'s multicellular chain life cycle
171 (3), it has not been determined if their formation is developmentally essential. Δ*fliC* and Δ*motA*

172 mutations block rosette folding without affecting adhesion and provide test cases for possible
173 developmental consequences. We found that Δ*fliC* and Δ*motA* communities remained linear,
174 single-cell-wide chains and did not organize three-dimensional structures. These communities
175 were unstable and broke into smaller chains and individual cells (Fig. 3F & G). Additionally,
176 though wild-type chains attached to the imaging surface, Δ*fliC* and Δ*motA* were often impaired for
177 attachment (Fig. S37-38; Movie S24). These results demonstrate that rosette formation is critical
178 to chain morphogenesis and surface attachment, and could suggest a role in biofilms as well. To
179 test this, we imaged hydrostatic Δ*fliC* and Δ*motA* biofilms at cellular scale (8) and found that wild-
180 type parallel-aligned, clonal-chain structure was abolished (Fig. 3H-J). Hence, *E. coli* rosettes are
181 critical to the development of multicellular chains and clonal-chain biofilms. This may partly
182 explain the requirement of flagella in hydrostatic *E. coli* biofilms (19, 20). Though motility may
183 contribute to biofilms in a variety of ways, our findings suggest swimming is incompatible with
184 rosette formation and subsequent multicellular chains and clonal-chain biofilms.

185 This study reveals a simple model for rosette formation in *E. coli*. Individual cells divide
186 and their daughter cells adhere to each other at their new poles. ~10 minutes later, sister cells
187 reposition themselves within seconds into parallel alignment (Fig. 1). This folding follows an
188 angular random walk (Fig. 1D-I) produced by the flagellum (Fig. 2). Parallel-aligned cells then
189 divide and further fold to produce 4-cell quatrefoil rosettes. The resulting space-enclosed
190 configuration is subsequently maintained by ECM production (3), facilitating the development of
191 multicellular chains and clonal-chain biofilms (Fig. 3G-I). *de novo* flagella synthesis is important
192 for rosette formation as the force of mature flagella can separate sister cells (Fig. 2K, 3A-D). In
193 total, *E. coli* self-organizes rosettes by combining adherence and flagella-mediated repositioning
194 of sister cells. Medically, *E. coli* is key in the gut microbiome and is responsible for 80% of UTIs,

195 which more than half of US women experience at least once in their lives. In the future, the
196 mechanism we have reported could be used to target rosette formation in order to re-program
197 microbiota or halt pathogenesis. Additionally, it might be used to improve existing antibiotics,
198 similar to metabolic potentiation of aminoglycoside against biofilms (30-33).

199 This study also has implications for the evolution of multicellular development. In *E. coli*,
200 thousands of multicellular chains, the result of a microscopic life cycle, can create macroscopic
201 biofilms (3). This life cycle, revealed by new methods for tracking individual cells, may be unique
202 to *E. coli,* though other species perform similar phenomena. For example, a *Bacillus subtilis* strain
203 produces biofilms by multicellular chain morphogenesis (34) which is maintained by ECM
204 production (35) and has genetically-regulated stages (36). Also, biofilms of a *P. aeruginosa* strain
205 are composed of parallel-aligned, clonal chains which are disrupted by removing biofilm genes
206 (37). Tracking cell motion will clarify the similarities between these bacteria, though their
207 behaviors add to evidence that microbes can satisfy basic developmental criteria (38). Beyond
208 these criteria, this study is the first time a bacterium has been shown to form clonal rosettes with
209 developmental consequences through sister-cell repositioning, similar in principle to multicellular
210 organisms. Hence, our findings support a subtle revision of the hypothesis that rosettes define
211 multicellular *organisms* (1) and indicate that they may be definitional to multicellular *development*
212 more broadly. As rosette formation efficiently establishes a channel for internal communication
213 amongst sister cells, it may represent an easily-executed, generative strategy for developmental
214 behavior. This idea further suggests that complex problems in the evolution and engineering of
215 *multicellularity* may be reducible to simpler questions concerning rosettes.

216 ## Materials and Methods

217 ### Strains, Plasmids, and Media

218 *Escherichia coli* MG1655 was the primary strain used in all experiments. *E. coli* AW405 strains
219 were also used where specified. To facilitate computational image processing and analysis and
220 also biofilm imaging, *E. coli* cells were transformed with pUA66-p*ompC*::*gfp* (green) (39) or
221 pEB2-mScarlet (red) (40). These plasmids constitutively-expressed fluorescent proteins and had
222 no observable effects on cellular behaviors. The Δ*fliC*, Δ*motA*, Δ*cheZ*, and Δ*cheY* strains were
223 created by transducing Δ*fliC*::kan(kanR), Δ*motA*::kan(kanR), Δ*cheZ*::kan(kanR), and
224 Δ*cheY*::kan(kanR) respectively from the KEIO Collection (41) using *P1vir* in *E. coli* MG 1655
225 following standard methods (42), and were cured with pCP20 (43). All strains were cultured in
226 LB, Miller broth at 37°C and with shaking at 300 RPM, in 14 mL Falcon Round-Bottom Test
227 Tubes with aerating caps (VWR), and in light-insulated shakers. Glucose (+) experiments used
228 Neidhardt Supplemented MOPS Defined Medium (EZ-rich; Teknova). When necessary, plasmids
229 were maintained by supplementing media with 50 μg/mL of kanamycin.

230

231 ### Cell Tracking Approach

232 LB agarose pads were built using 2% agarose, following standard methods (44) but with described
233 modifications (3). 3 μL exponential phase cells were added to agarose pads, which were
234 immediately covered with cover glass and were not allowed to dry. For glucose transition
235 experiments, *E. coli* AW405 cells were cultured overnight in Neidhardt Supplemented MOPS
236 Defined Medium (EZ-rich; Teknova) and loaded onto LB-2% agarose pads for tracking cell
237 dynamics. Dynamic bright field imaging was typically conducted at 2-second resolution.

238 Dynamical fluorescent imaging was performed at 30-second resolution (instead of 2-second) to
239 avoid the confounding effects of exposing bacteria to high-intensity blue light.
240
241 **Microscopy**
242 Images were acquired using a Leica DMi8 microscope equipped with a DIC HCPL APO 63X oil
243 immersion objective (1.6 mag changer), Hamamatsu ORCA-Flash 4.0 camera, and Lumencor
244 Spectra-X light engine. Devices for imaging were placed in a microscope-stage-top incubator
245 (Tokai-Hit, STX Stage Top Incubator Temp and Flow; STXF-WSKMX-SET), and temperature
246 was maintained at 37°C throughout image acquisition using a stage-top incubator (Tokai-Hit).
247 Time courses were collected in an automated manner using the Leica LasX software at specified
248 time intervals and at 100x magnification. Imaging was performed using differential interference
249 contrast (DIC) and fluorescence channels. Excitation and emission for fluorescence microscopy
250 was performed at 470 nm and 500-550 nm for green fluorescence and 510 nm and 592-668 nm for
251 red fluorescence respectively. AW405 flagella were stained as previously described (28) with
252 Alexa Fluor 488. Real-time staining of *de novo* flagella synthesis by Alexa Fluor 488 was
253 attempted and has not been previously reported. Biofilm imaging experiments were performed as
254 previously described (8). Biofilm inoculum consisted of a 1:10 mixture of cells containing
255 pUA66-p*ompC*::*gfp* (green) and pEB2-mScarlet (red) in 96-well microtiter plates. Plates, with
256 cover glass pieces inserted in wells, were incubated without shaking overnight at 37°C then imaged
257 at 100x magnification. Micrograph examples and movies were generated using Leica X software.
258
259

260 **Image Analysis**

261 For analysis of images of cell dynamics captured using green fluorescent channel, raw images
262 were segmented using custom MATLAB scripts to calculate the angle between sister cells during
263 cell folding and their angular velocity. Higher resolution images of cells captured using DIC were
264 first processed in ImageJ to manually mark the poles for both the sister cells. Coordinates for the
265 pole positions were then loaded into MATLAB for calculating motion. θ was determined as the
266 2D angle between the two sister cells, and these values were also used to determine the angular
267 velocity. Φ represented the angle between a cell and the imaging surface, in the z direction (toward
268 the camera). This was calculated by trigonometry from the 2-D projection of the cell and its
269 calculated length immediately prior to folding. As folding occurred within seconds, the cell length
270 was treated as constant for angle calculations. Strokes were identified as motion > 0.8 μm between
271 consecutive time points. δ was calculated as the angle between the vectors of two separate strokes.
272 Figures were arranged and formatted using Adobe Illustrator.

273

274

275 **Acknowledgements**

276 We are grateful to Howard C. Berg and Karen Fahrner for sharing AW405 strains and methods
277 and Philippe Cluzel for sharing pEB2-mScarlet. This study was supported by an NIH Director's
278 Early Independence Award (DP5OD019792) to Kyle R. Allison.

References

1. Brunet T & King N (2017) The Origin of Animal Multicellularity and Cell Differentiation. *Dev Cell* 43(2):124-140.
2. O'Toole G, Kaplan HB, & Kolter R (2000) Biofilm formation as microbial development. *Annu Rev Microbiol* 54:49-79.
3. Puri D, Fang X, & Allison KR (2023) Evidence of a possible multicellular life cycle in Escherichia coli. *iScience* 26(1):105795.
4. Moore RL & Marshall KC (1981) Attachment and rosette formation by hyphomicrobia. *Appl Environ Microbiol* 42(5):751-757.
5. Ong CJ, Wong ML, & Smit J (1990) Attachment of the adhesive holdfast organelle to the cellular stalk of Caulobacter crescentus. *J Bacteriol* 172(3):1448-1456.
6. Keim CN*, et al.* (2004) Multicellular life cycle of magnetotactic prokaryotes. *FEMS Microbiol Lett* 240(2):203-208.
7. Justice SS*, et al.* (2004) Differentiation and developmental pathways of uropathogenic Escherichia coli in urinary tract pathogenesis. *Proc Natl Acad Sci U S A* 101(5):1333-1338.
8. Puri D, Fang X, & Allison KR (2023) Fluorescence-based protocol for revealing cellular arrangement in biofilms. *STAR Protoc* 4(2):102270.
9. Datta A, Bryant DM, & Mostov KE (2011) Molecular regulation of lumen morphogenesis. *Curr Biol* 21(3):R126-136.
10. Mysorekar IU & Hultgren SJ (2006) Mechanisms of uropathogenic Escherichia coli persistence and eradication from the urinary tract. *Proc Natl Acad Sci U S A* 103(38):14170-14175.
11. Alon U, Surette MG, Barkai N, & Leibler S (1999) Robustness in bacterial chemotaxis. *Nature* 397(6715):168-171.
12. Korobkova E, Emonet T, Vilar JM, Shimizu TS, & Cluzel P (2004) From molecular noise to behavioural variability in a single bacterium. *Nature* 428(6982):574-578.
13. Korobkova EA, Emonet T, Park H, & Cluzel P (2006) Hidden stochastic nature of a single bacterial motor. *Phys Rev Lett* 96(5):058105.
14. Berg HC (1984) (Princeton University Press, Princeton).
15. Berg HC (2004) (Springer New York, New York, NY).
16. Codling EA, Plank MJ, & Benhamou S (2008) Random walk models in biology. *J R Soc Interface* 5(25):813-834.
17. Berg HC (2003) The rotary motor of bacterial flagella. *Annu Rev Biochem* 72:19-54.
18. Macnab RM (2003) How bacteria assemble flagella. *Annu Rev Microbiol* 57:77-100.
19. Pratt LA & Kolter R (1998) Genetic analysis of Escherichia coli biofilm formation: Roles of flagella, motility, chemotaxis and type I pili. *Molecular Microbiology* 30(2):285-293.
20. Niba ET, Naka Y, Nagase M, Mori H, & Kitakawa M (2007) A genome-wide approach to identify the genes involved in biofilm formation in E. coli. *DNA Res* 14(6):237-246.
21. Dayel MJ*, et al.* (2011) Cell differentiation and morphogenesis in the colony-forming choanoflagellate Salpingoeca rosetta. *Dev Biol* 357(1):73-82.
22. Parkinson JS (1978) Complementation analysis and deletion mapping of Escherichia coli mutants defective in chemotaxis. *J Bacteriol* 135(1):45-53.
23. Parkinson JS, Parker SR, Talbert PB, & Houts SE (1983) Interactions between chemotaxis genes and flagellar genes in Escherichia coli. *J Bacteriol* 155(1):265-274.
24. Laganenka L, Colin R, & Sourjik V (2016) Chemotaxis towards autoinducer 2 mediates autoaggregation in Escherichia coli. *Nat Commun* 7:12984.
25. Suchanek VM*, et al.* (2020) Chemotaxis and cyclic-di-GMP signalling control surface attachment of Escherichia coli. *Mol Microbiol* 113(4):728-739.

26. Pruss BM & Matsumura P (1997) Cell cycle regulation of flagellar genes. *J Bacteriol* 179(17):5602-5604.
27. Fahrner KA & Berg HC (2015) Mutations That Stimulate flhDC Expression in Escherichia coli K-12. *J Bacteriol* 197(19):3087-3096.
28. Turner L, Ryu WS, & Berg HC (2000) Real-time imaging of fluorescent flagellar filaments. *J Bacteriol* 182(10):2793-2801.
29. Schembri MA & Klemm P (2001) Biofilm formation in a hydrodynamic environment by novel FimH variants and ramifications for virulence. *Infection and Immunity*.
30. Allison KR, Brynildsen MP, & Collins JJ (2011) Metabolite-enabled eradication of bacterial persisters by aminoglycosides. *Nature* 473(7346):216-220.
31. Rosenberg CR, Fang X, & Allison KR (2020) Potentiating aminoglycoside antibiotics to reduce their toxic side effects. *PLoS One* 15(9):e0237948.
32. Barraud N, Buson A, Jarolimek W, & Rice SA (2013) Mannitol enhances antibiotic sensitivity of persister bacteria in Pseudomonas aeruginosa biofilms. *PLoS One* 8(12):e84220.
33. Meylan S*, et al.* (2017) Carbon Sources Tune Antibiotic Susceptibility in Pseudomonas aeruginosa via Tricarboxylic Acid Cycle Control. *Cell Chem Biol* 24(2):195-206.
34. Branda SS, Gonzalez-Pastor JE, Ben-Yehuda S, Losick R, & Kolter R (2001) Fruiting body formation by Bacillus subtilis. *Proc Natl Acad Sci U S A* 98(20):11621-11626.
35. van Gestel J, Vlamakis H, & Kolter R (2015) Division of Labor in Biofilms: the Ecology of Cell Differentiation. *Microbiol Spectr* 3(2):MB-0002-2014.
36. Kobayashi K (2007) Bacillus subtilis pellicle formation proceeds through genetically defined morphological changes. *J Bacteriol* 189(13):4920-4931.
37. Dayton H*, et al.* (2023) Cell arrangement impacts metabolic activity and antibiotic tolerance in Pseudomonas aeruginosa biofilms. *bioRxiv*:2023.2006.2020.545666.
38. Monds RD & O'Toole GA (2009) The developmental model of microbial biofilms: ten years of a paradigm up for review. *Trends Microbiol* 17(2):73-87.
39. Zaslaver A*, et al.* (2006) A comprehensive library of fluorescent transcriptional reporters for Escherichia coli. *Nature Methods*.
40. Balleza E, Kim JM, & Cluzel P (2018) Systematic characterization of maturation time of fluorescent proteins in living cells. *Nature Methods* 15(1):47-51.
41. Baba T*, et al.* (2006) Construction of Escherichia coli K-12 in-frame, single-gene knockout mutants: The Keio collection. *Molecular Systems Biology* 2.
42. Thomason LC, Costantino N, & Court DL (2007) E. coli Genome Manipulation by P1 Transduction.), pp 1.17.11-11.17.18.
43. Datsenko KA & Wanner BL (2000) One-step inactivation of chromosomal genes in Escherichia coli K-12 using PCR products. *Proc Natl Acad Sci U S A* 97(12):6640-6645.
44. Young JW*, et al.* (2012) Measuring single-cell gene expression dynamics in bacteria using fluorescence time-lapse microscopy. *Nature Protocols* 7(1):80-88.

Figures

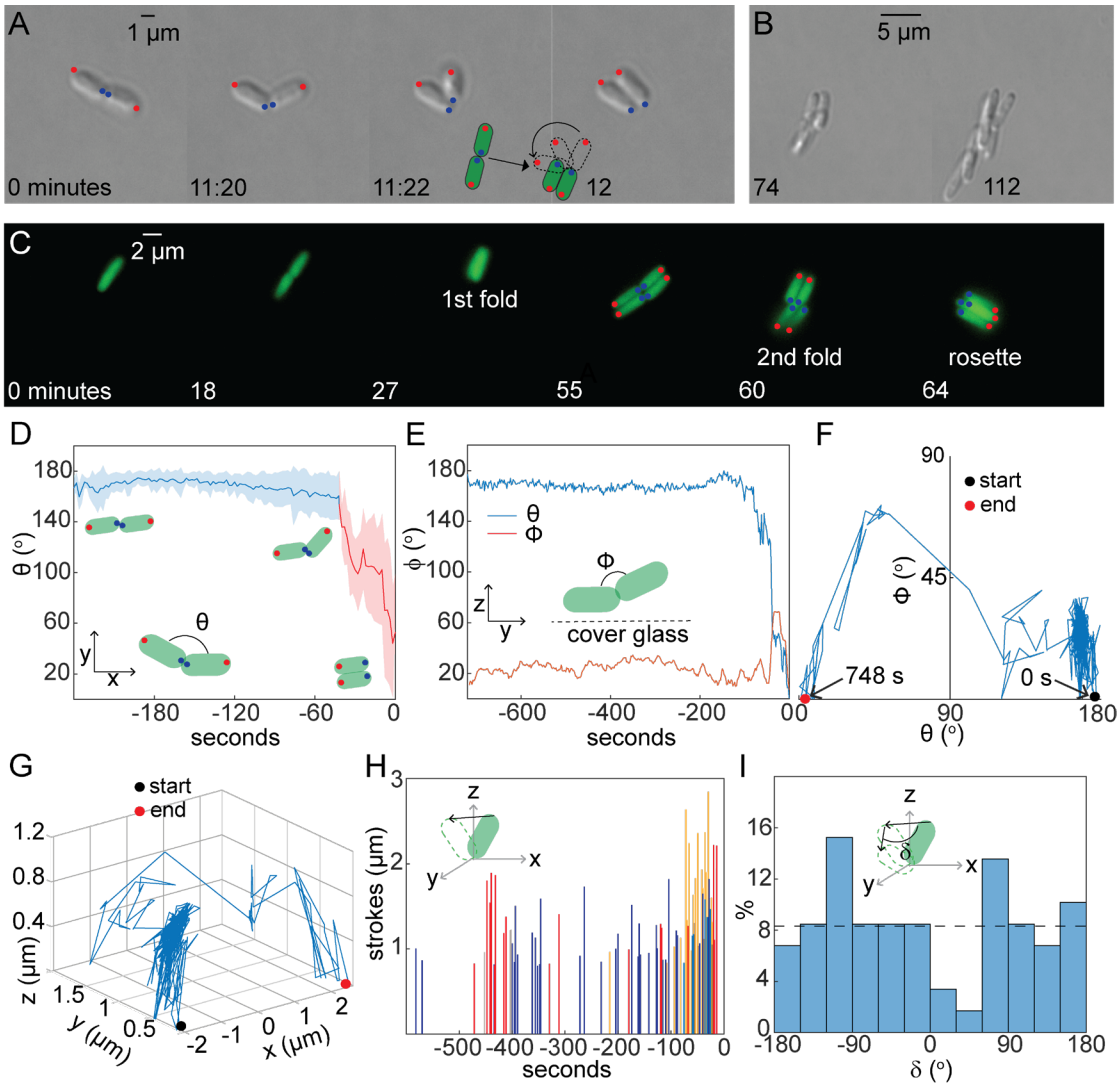

Figure 1. Sister-cell folding produces rosettes and follows an angular random walk. (A) Micrographs from a representative movie (2-second resolution) of *E. coli* sister-cell folding and parallel alignment. Time and scale indicated on all micrographs. New (blue) and old (red) poles are indicated. Inset: illustration of cell folding documented in movies. (B) Later micrographs from the same video. (C) Micrographs from a representative movie (30-second resolution) of rosette formation in cells constitutively-expressing GFP. New (blue) and old (red) poles are indicated. (D) Dynamics of sister-cell angle (θ) during cellular folding (2-second resolution; mean ± standard deviation, n=5). Folding (red) and pre-folding (blue) are indicated. Inset: illustration of θ calculation. (E) Representative example of sister cell θ (blue) and Φ (red). Inset: illustration of Φ calculation. (F) Trajectory of sister-cell angles from representative example of folding. Start and end positions and times are indicated. (G) Representative example of 3D trajectory of cell pole during folding. (H) Dynamics of angular strokes (movement >0.8 μm) for 4 representative sister-cell pairs. Inset: illustration of distance calculation. (I) Distribution of angle change between strokes (δ) (n=59). Inset: illustration of δ calculation.

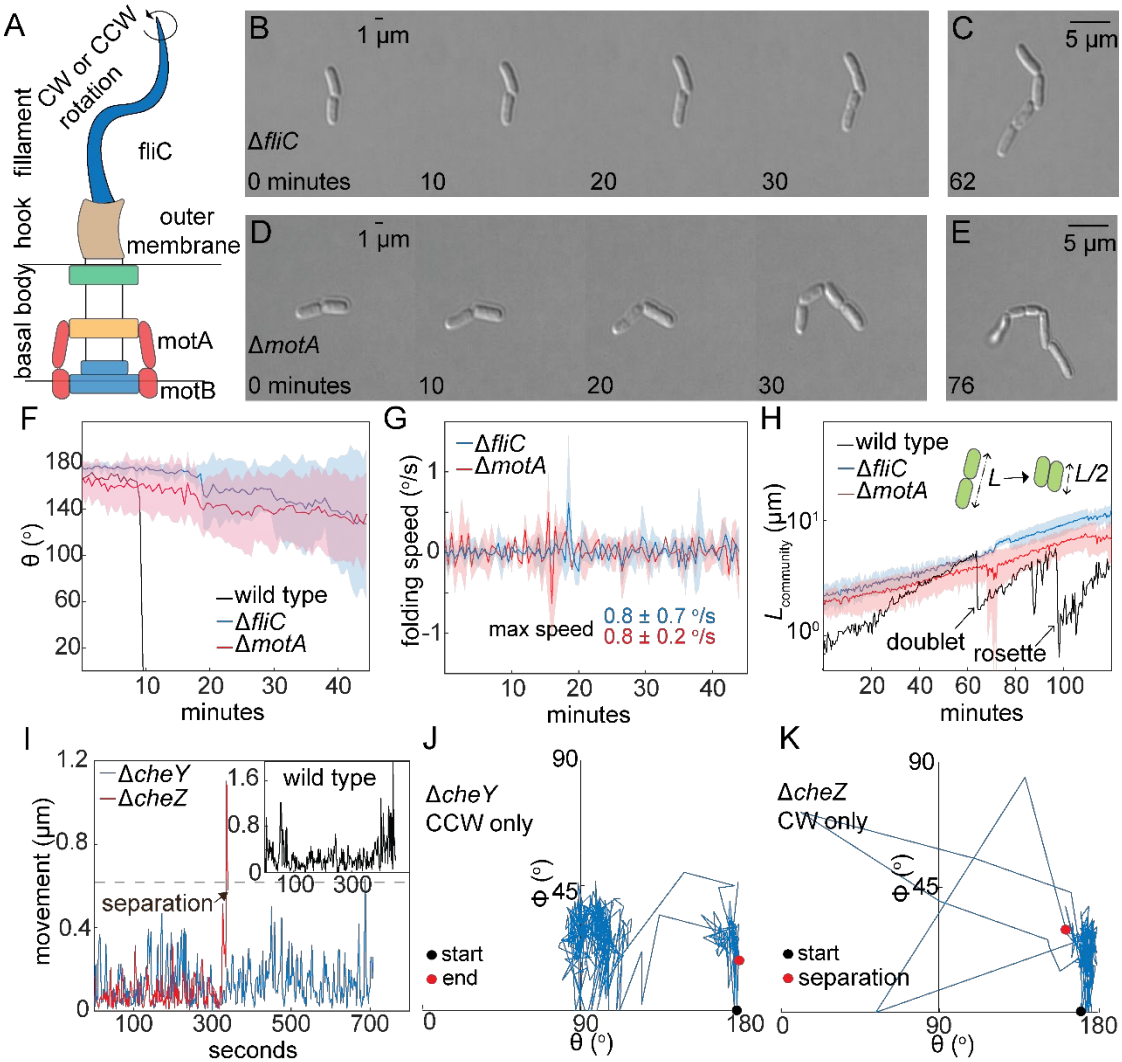

Figure 2. Flagella propulsion generates sister cell folding. (A) Diagram of the flagellum (not to scale). Micrographs from representative movies of (B) Δ*fliC* and (D) Δ*motA* cells. Time and scale indicated on all micrographs. Later micrographs of (C) Δ*fliC* and (E) Δ*motA* cells from the same videos. (F) Dynamics of Δ*fliC* (blue) and Δ*motA* (red) sister-cell angle (30-second resolution; mean ± standard deviation, n=3). An example wild-type trajectory is included for comparison. (G) Dynamics of angular speed for Δ*fliC* and Δ*motA* cells (30-second resolution; mean ± standard deviation, n=3). Inset: average maximum speed during. (H) Length dynamics of Δ*fliC* and Δ*motA* communities (mean ± standard deviation; n= 3). An example wild-type trajectory is included for comparison. Inset: illustration of halving length during folding. (I) Dynamics of angular movement for representative Δ*cheY* (blue) and Δ*cheZ* (red) sister-cell pairs (2-second resolution). Inset: representative wild-type example. (J) Trajectory of sister-cell angles from representative Δ*cheY* example. (K) Trajectory of sister-cell angles from representative Δ*cheZ* example.

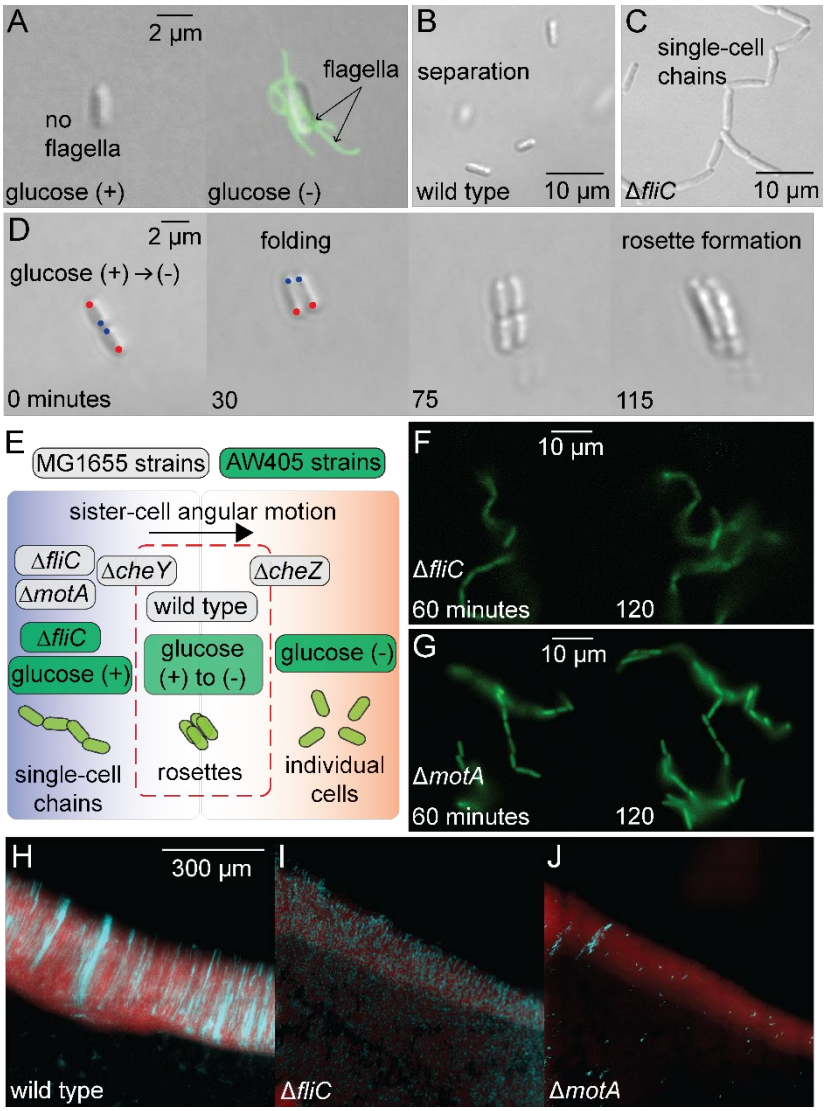

Figure 3. Rosettes require *de novo* flagella and have developmental consequences. (A) Representative micrographs of AW405 cells grown (left) with glucose and (right) without glucose and stained with Alexa Fluor 488 (green). Scale indicated on all micrographs. Micrographs from representative movies of (B) AW405 and (C) AW405 Δ*fliC* cells grown without glucose. (D) Micrographs from a representative movie of AW405 transitioned from glucose (+) to glucose (-) media. New (blue) and old (red) poles are indicated. (E) Diagram of the relative sister-cell angular motion of strains and conditions in this study revealing its ability to predict the structure of multicellular communities. Δ*cheY* and Δ*cheZ* cells produce heterogeneous outcomes and hence overlap depicted multicellular regions. Micrographs from representative movies of (F) Δ*fliC* and (G) Δ*motA* cells constitutively-expressing GFP (30-second resolution) depicting long-term lack of community structure. Time and scale are indicated. Micrographs of biofilms formed by (H) wild-type, (I) Δ*fliC*, and (J) Δ*motA* cells. Cells contained either mScarlet (red) or GFP (cyan) at a 10:1 ratio.